

## Electronic transport and atomic vibrational properties of semiconducting $\text{Mg}_2^{119}\text{Sn}$ thin film

B. SAHOO\*<sup>†</sup>, W. A. ADEAGBO<sup>†</sup>, F. STROMBERG<sup>†</sup>, W. KEUNE<sup>†</sup>,  
E. SCHUSTER<sup>†</sup>, R. PETERS<sup>†</sup>, P. ENTEL<sup>†</sup>, S. LÜTTJOHANN<sup>†</sup>,  
A. GONDORF<sup>†</sup>, W. STURHAHN<sup>‡</sup>, J. ZHAO<sup>‡</sup>, T. S. TOELLNER<sup>‡</sup>  
and E. E. ALP<sup>‡</sup>

<sup>†</sup>Department of Physics, University of Duisburg-Essen,  
D-47048 Duisburg, Germany

<sup>‡</sup>Advanced Photon Source, Argonne National Laboratory,  
Argonne, IL 60439, USA

(Received 1 July 2006; in final form 17 October 2006)

A polycrystalline  $\text{Mg}_2\text{Sn}$  thin film has been prepared by thermal co-evaporation in ultrahigh vacuum of Mg and Sn onto a naturally oxidized Si(100) substrate at  $-140^\circ\text{C}$ . The structure of the sample was characterized by X-ray diffraction (XRD) and  $^{119}\text{Sn}$  conversion electron Mössbauer spectroscopy (CEMS). The semiconducting property of the  $\text{Mg}_2\text{Sn}$  thin film was confirmed by electrical resistance, magnetoresistance, Hall-effect and infrared spectroscopy measurements, and a value of  $\sim 0.2\text{ eV}$  was found for the electronic gap energy. The  $^{119}\text{Sn}$ -projected partial vibrational density of states (VDOS),  $g(E)$ , has been measured by nuclear resonant inelastic X-ray scattering (NRIXS) of 23.878 keV synchrotron radiation. Together with  $g(E)$ , other thermodynamic quantities such as the probability of recoilless absorption ( $f$ -factor), the average kinetic energy per Sn atom, the average force constant, and the vibrational entropy per Sn atom are obtained. The partial VDOS of both elements (Mg and Sn) has been calculated theoretically and reasonable agreement with the measured  $^{119}\text{Sn}$ -projected VDOS is observed.  $g(E)$  is characterized by a phonon energy gap ranging from  $\sim 17$  to  $\sim 21\text{ meV}$ .

*Keywords:*  $\text{Mg}_2\text{Sn}$  film;  $^{119}\text{Sn}$  Mössbauer spectroscopy; Hall effect; Infrared spectroscopy; Nuclear resonant inelastic X-ray scattering; Phonon density of states; *Ab-initio* calculation

### 1. Introduction

Magnesium stannide,  $\text{Mg}_2\text{Sn}$ , is a narrow-gap semiconductor with an energy gap of about 0.3 eV [1, 2]. It has fluorite-type cubic crystal structure with a lattice constant  $a = 6.763\text{ \AA}$  [1].  $\text{Mg}_2\text{Sn}$  has similar electronic properties like  $\alpha\text{-Sn}$  [3]. Piezoresistance measurements have been performed on  $\text{Mg}_2\text{Sn}$  [4, 5] which suggest

---

\*Corresponding author. Tel.: 0049 203 379 2955. Fax: 0049 203 379 3601. Email: balaram\_sahoo@uni-duisburg.de

a many-valley-type conduction band and a carrier mobility insensitive to changes in sample volume. The lattice vibrational properties of  $\text{Mg}_2\text{Sn}$  have already been studied by inelastic neutron scattering [6]. Several theoretical and experimental studies on vibrational properties of  $\text{Mg}_2\text{Sn}$  has been performed [6–10]. However, the study of the vibrational density of states (VDOS),  $g(E)$ , and related phenomena in thin films and multilayers by inelastic neutron scattering is not feasible with present neutron sources. On the other hand, nuclear resonant inelastic X-ray scattering (NRIXS) of synchrotron radiation is proven to be a valuable tool for the direct measurement of the partial VDOS and other related quantities of the resonant nuclei [11–15]. Because of the capability to measure buried interfaces even on the nanoscale, NRIXS has opened a new dimension for the study of lattice dynamics of thin films, interfaces and multilayers [16–29]. In the present work results from infrared spectroscopy, electrical resistance, Hall effect measurements,  $^{119}\text{Sn}$  Mössbauer spectroscopy and  $^{119}\text{Sn}$  nuclear resonant inelastic X-ray scattering on a polycrystalline 800 Å thick  $\text{Mg}_2\text{Sn}$  thin film will be reported. The vibrational properties of  $\text{Mg}_2\text{Sn}$  obtained by NRIXS and by ab-initio calculations will be extensively covered.

## 2. Sample preparation and characterization

The  $\text{Mg}_2\text{Sn}$  thin film sample (800 Å thick) was prepared by co-deposition of Mg and Sn (82.9% isotopical enrichment in  $^{119}\text{Sn}$ ) onto an oxidized Si(100) substrate held at  $-140^\circ\text{C}$ . Prior to deposition the substrate was cleaned by acetone followed by propanol. The substrate was then heated in ultrahigh vacuum (UHV) to about  $450^\circ\text{C}$  to remove adsorbed contaminants from the surface. The deposition was carried out in an UHV system with a base pressure of  $5 \times 10^{-10}$  m bar. The pressure during deposition was  $\sim 3 \times 10^{-9}$  m bar. The substrate temperature ( $T_s$ ) was kept constant at  $-140^\circ\text{C}$ . The deposition rates were 0.35 and  $0.185 \text{ \AA s}^{-1}$  for Mg and Sn, respectively. In order to achieve stoichiometry a slightly higher evaporation rate for Mg serves for the compensation of the low sticking coefficient of Mg. The purity of Mg and Sn was 99.999 and 99.995%, respectively. The deposition rates, and simultaneously the sample thickness, were monitored by calibrated quartz crystal oscillators and controlled by a personal computer. The sample was finally covered by 50 Å Cr for protection against oxidation.

The structure of the sample was characterized by conventional  $\theta$ - $2\theta$  X-ray diffraction (XRD) and  $^{119}\text{Sn}$  conversion electron Mössbauer spectroscopy (CEMS). For the XRD measurements Cu- $K\alpha$  radiation and a graphite monochromator were used. Interestingly, instead of the expected formation of an amorphous Mg–Sn alloy, the crystalline  $\text{Mg}_2\text{Sn}$  phase is formed even at this low preparation temperature ( $T_s = -140^\circ\text{C}$ ). Figure 1 shows the XRD pattern of the 800 Å thick  $\text{Mg}_2\text{Sn}$  film on oxidized Si(100). The presence of (111), (220), (311), and (222) Bragg peaks of  $\text{Mg}_2\text{Sn}$  indicates the polycrystalline nature of the film with a measured lattice constant  $a = 6.732 \text{ \AA}$  which is slightly smaller than that of bulk  $\text{Mg}_2\text{Sn}$  ( $a = 6.763 \text{ \AA}$ ). The CEM spectrum was measured at room temperature by placing the sample into a He + 4%  $\text{CH}_4$  proportional counter with the film surface perpendicular to the incident 23.878 keV  $\gamma$ -ray of the  $^{119}\text{Sn}^*$  source ( $\text{CaSnO}_3$ -matrix). The spectrum was least-squares fitted by a single Lorentzian line. For the

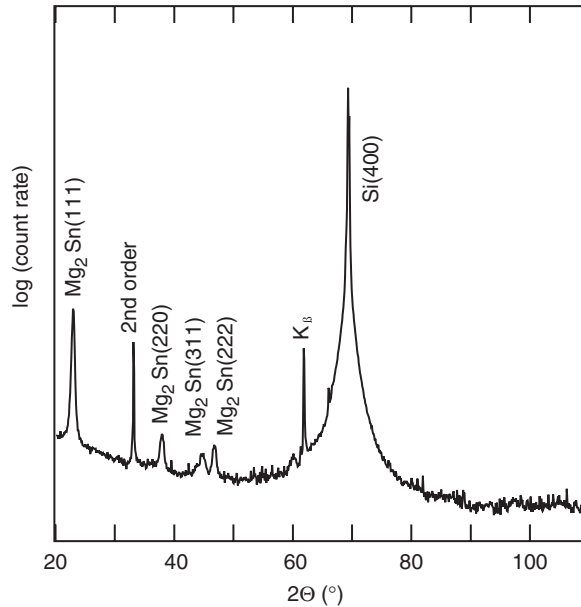


Figure 1. X-ray diffraction pattern of 800 Å thick  $\text{Mg}_2\text{Sn}$  thin film grown on an oxidized Si(100) substrate at  $T_s = -140^\circ\text{C}$ . Cu- $\text{K}\alpha$  radiation was used.  $\text{K}_\beta$  means: Si(400)-Cu- $\text{K}\beta$  peak, and 2nd order means: Si(400)-Cu- $\text{K}\alpha$ , 2nd order reflection. The  $\text{Mg}_2\text{Sn}$  Bragg peaks are clearly observed.

least-squares fitting of the CEM spectrum, the computer program *NORMOS* by Brand [30] was used.

### 3. Mössbauer spectroscopical results

A  $^{119}\text{Sn}$  CEMS study on  $\text{Mg}_2\text{Sn}$  thin films has not been reported yet. Only one report describing transmission Mössbauer spectroscopy on bulk  $\text{Mg}_2\text{Sn}$  exists [31]. The reported isomer shift (relative to a  $\text{SnO}_2$  source) ( $\delta$ ) for bulk  $\text{Mg}_2\text{Sn}$  is  $1.860(5)\text{mm s}^{-1}$ , which is slightly less than that of  $\alpha\text{-Sn}$  ( $\delta = 2.012\text{mm s}^{-1}$ ). As the change of the isomer shift originates from the difference in the  $s$ -electron density at the  $^{119}\text{Sn}$  nucleus, which causes a shift of the nuclear levels, the slightly lower isomer shift (or reduced  $s$ -electron density at the  $^{119}\text{Sn}$  nucleus) of  $\text{Mg}_2\text{Sn}$  in comparison to  $\alpha\text{-Sn}$  can be understood as follows.  $\text{Mg}_2\text{Sn}$  has practically the same  $s$ -electron content per Sn atom as  $\alpha\text{-Sn}$  (about 1.4) [3]. However, the Sn sphere in  $\text{Mg}_2\text{Sn}$  has accommodated more  $p$ -electrons than in  $\alpha\text{-Sn}$ . This causes a charge transfer towards the Sn atom (in  $\text{Mg}_2\text{Sn}$ ) making Sn more electronegative than Mg. Hence, Sn plays the role of an anion in this compound, although  $\text{Mg}_2\text{Sn}$  is highly covalent in character. The charge-pile-up at Sn atoms occurs mainly in the outermost region of the Sn sphere having  $p$ -character. The resulting lower  $s$ -electron contact density at the  $^{119}\text{Sn}$  nucleus in comparison to  $\alpha\text{-Sn}$  occurs because of the increased shielding of the  $s$ -electrons by  $p$ -electrons. Figure 2 shows the  $^{119}\text{Sn}$  CEM spectrum of the 800 Å thick  $\text{Mg}_2\text{Sn}$  film measured at RT. Our observed isomer shift

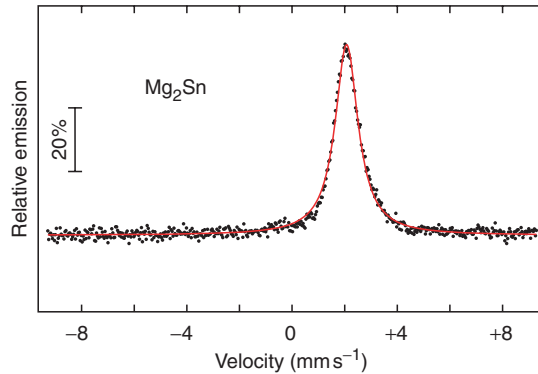


Figure 2. RT  $^{119}\text{Sn}$  Mössbauer spectrum of  $\text{Mg}_2\text{Sn}$  thin film grown at  $T_s = -140^\circ\text{C}$ . The spectrum was least-squares fitted by a single Lorentzian line as shown by the full-drawn line. The line width (FWHM) measured is  $1.06 \text{ mm s}^{-1}$ .

(relative to the  $\text{CaSnO}_3$  source)  $\delta = 2.07(5) \text{ mm s}^{-1}$  for the  $\text{Mg}_2\text{Sn}$  film is almost equal to the isomer shift of  $\alpha\text{-Sn}$ . This confirms the same  $s$ -electron contact density for  $\alpha\text{-Sn}$  and the  $\text{Mg}_2\text{Sn}$  film. It seems that the  $s$ -electron screening due to the  $p$ -electron charge cloud is somewhat less effective in our polycrystalline thin film. This might be due to a small degree of atomic disorder in the  $\text{Mg}_2\text{Sn}$  film, as can be inferred also from the enlarged linewidth of the  $\text{Mg}_2\text{Sn}(311)$  Bragg peak (Fig. 1), or could be caused by the smaller lattice parameter of the film as compared to the bulk. The measured Mössbauer linewidth (FWHM) in figure 2 is  $1.06 \text{ mm/s}$ , which is larger than the natural linewidth of  $0.646 \text{ mm s}^{-1}$  for  $^{119}\text{Sn}$  [32]. This excess line broadening may be caused by an unresolved distribution of isomer shifts and/or quadrupole splittings due to inhomogeneous lattice distortions and/or some degree of atomic disorder.

#### 4. Semiconducting properties

Preliminary measurements of the electrical resistance, galvanomagnetic effects and infrared absorption have been performed in order to prove the semiconducting nature of the  $\text{Mg}_2\text{Sn}$  film. The semiconducting property of our film (as described below) provides motivation for future experimental and theoretical investigations of thin films and multilayers containing  $\text{Mg}_2\text{Sn}$ .

##### 4.1. Electrical resistance

The electrical resistance measurement on the  $\text{Mg}_2\text{Sn}$  film has been performed in a temperature range between 4.2 and 300 K by using a standard four-point probe method. The observed resistance of the film *versus* temperature is shown in figure 3. From the figure it is clear that the observed behavior is neither that of a pure metal nor that of a pure semiconductor. The behavior at low temperature ( $<150 \text{ K}$ ) indicates dominant metallic character. However, the high temperature ( $>150 \text{ K}$ ) electrical resistance,  $R$ , decreases with increasing temperature which is typical semiconducting behavior. Considering the sample structure, it is apparent that the observed resistance-*versus*- $T$  behavior is a combined effect of the metallic  $60 \text{ \AA}$  thick

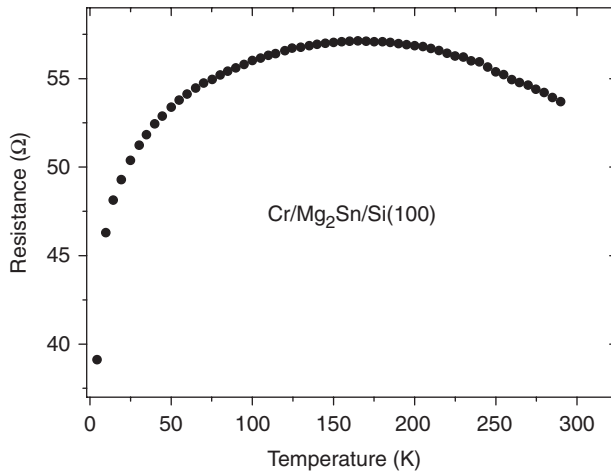


Figure 3. Electrical resistance *vs.* temperature of  $\text{Mg}_2\text{Sn}$  thin film.

Cr coating layer and the semiconducting  $800 \text{ \AA}$  thick  $\text{Mg}_2\text{Sn}$  layer. At low temperature ( $<150 \text{ K}$ ) the resistance of the metallic Cr layer is much smaller than the high resistance of the semiconducting  $\text{Mg}_2\text{Sn}$  layer, hence most of the applied current flows through the Cr layer providing metallic-like low temperature behavior. However, when the temperature increases the electrons from the valence band of the semiconductor are thermally excited to the conduction band, thus decreasing the resistance of the semiconducting layer. Simultaneously the resistance of the metallic Cr layer increases with temperature and the current flowing through this layer decreases. Hence, the observed behavior of the sample is a competition between the metallic character of the Cr film and the semiconducting character of the  $\text{Mg}_2\text{Sn}$  film. The decrease of the resistance at high temperature ( $>170 \text{ K}$ ) indicates that in this temperature range the major contribution to the conductance is provided by the semiconducting  $\text{Mg}_2\text{Sn}$  layer. Further, an estimation of the effective band gap from the slope of the straight line produced by a plot of  $\ln(R)$  *versus*  $1/T$  for our sample, as described in [1,33], resulted in an about one order-of-magnitude smaller value than the band gap of bulk  $\text{Mg}_2\text{Sn}$ . However, the semiconducting property of our  $\text{Mg}_2\text{Sn}$  film is clearly proven by the  $R$ -*versus*- $T$  measurement (Figure 3).

#### 4.2. Galvanomagnetic effects

As the Hall effect is smaller for metals than for semiconductors, galvanomagnetic effects, in general, provide important results for the semiconductor and less so for the metal. We have performed preliminary galvanomagnetic measurements which also demonstrates the semiconducting nature of our  $\text{Mg}_2\text{Sn}$  film. The sample was found to exhibit almost no magnetoresistance ( $<0.1\%$ ) even at  $4.2 \text{ K}$  and up to a magnetic field of  $2T$ . Although similar results were reported earlier [34], this small magnetoresistance may be due to the influence of the top Cr-layer in our case. The Hall resistance measurement in a magnetic field of  $0.5T$  has been performed in a split-coil superconducting-magnet cryostat using the van der Pauw four-point probe method [35]. The obtained Hall resistance of our sample at different temperatures up to  $100 \text{ K}$  is given in figure 4. From this result we have calculated the carrier density and Hall mobility of our sample, as shown in figures 5 and 6, respectively. The results

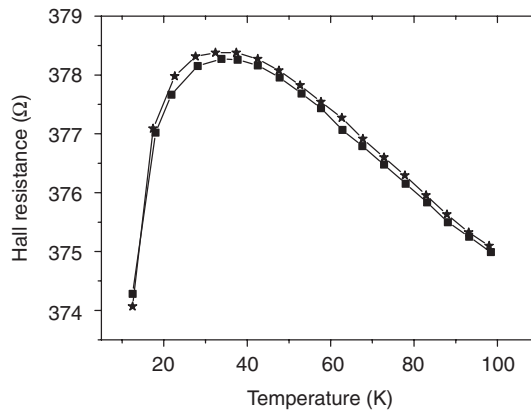


Figure 4. Hall resistance (at  $0.5T$  magnetic field and  $90\ \mu\text{A}$  current) vs. temperature of the  $\text{Mg}_2\text{Sn}$  film. The resistance represented by asterisks was measured at an opposite magnetic field direction with respect to the other data points represented by squares. The magnetic field was applied along the film-normal direction. (The full-drawn lines are guides for the eyes).

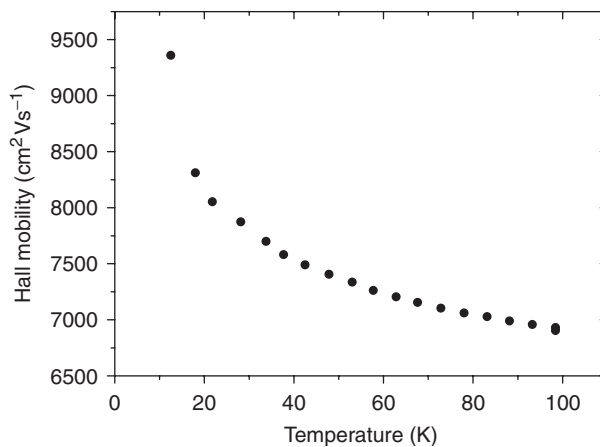


Figure 5. Carrier density vs. temperature of  $\text{Mg}_2\text{Sn}$  film.

show a carrier concentration of the sample of the order of  $2.02 \times 10^{18}\ \text{cm}^{-3}$ , and it turned out to be an n-type semiconductor, with electrons as major charge carriers. Clearly, the mobility decreases at higher temperatures (figure 6) following a  $T^{-1/2}$  law, indicating the importance of electron scattering with optical phonons. The behavior observed here is similar to results reported earlier [36, 37]. The decrease of the mobility with increasing temperature proves the semiconducting nature of our sample. However, the effect of the Cr-top layer in the sample was quite high and cannot be neglected.

### 4.3. Infrared absorption spectroscopy

Infrared absorption spectroscopy (transmission geometry) has been performed on the  $\text{Mg}_2\text{Sn}$  thin film sample and, for comparison, on an oxidized Si(100) substrate,

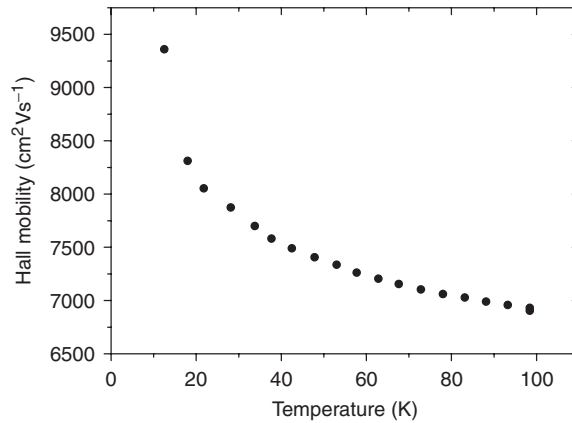


Figure 6. Hall mobility vs. temperature of  $\text{Mg}_2\text{Sn}$  film.

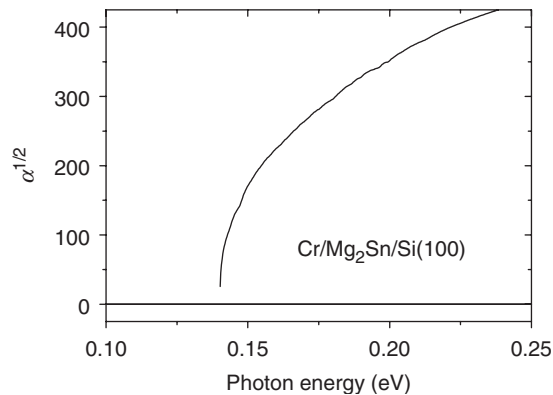


Figure 7. Square-root of light absorption coefficient vs. photon energy of the  $\text{Mg}_2\text{Sn}$  film on oxidized Si(100) substrate at room temperature. The band-gap energy is near 0.14 eV.

at room temperature (*RT*). The obtained transmission probability for the sample was divided by the transmission probability of the substrate in order to obtain the relative transmission of the sample as a function of photon energy. The absorption coefficient ( $\alpha$ ) has been calculated by using the Lambert–Beer’s law. The square-root of  $\alpha$  ( $\sqrt{\alpha}$ ) versus photon energy has been plotted in figure 7. This graph demonstrates that the band-gap energy is at about 0.14 eV. This value is smaller than band-gap energies reported earlier for bulk  $\text{Mg}_2\text{Sn}$  [38]. This discrepancy might be caused by the influence of the 60 Å Cr-coating layer, by defects or by lattice strain in our film.

## 5. Nuclear resonant inelastic X-ray scattering

The NRIXS experiments were performed at RT at the undulator beamline 3-ID of the Advanced Photon Source in Argonne (USA). The method of inelastic nuclear resonant absorption of 23.878 keV X-rays is selective to the  $^{119}\text{Sn}$  resonant isotope

and provides the Sn-projected (partial) VDOS rather directly with a minimum of modeling [12, 13]. Details of the technique are described elsewhere [11–18]. The monochromatized synchrotron radiation was incident onto the film surface under a grazing angle of  $\sim 4$  mrad and had an energy bandwidth (FWHM) of 0.9 meV. The X-ray beam was focussed to about  $10 \times 10 \mu\text{m}^2$  in size. The energy was tuned around the 23.878 keV nuclear resonance of  $^{119}\text{Sn}$  nuclei. Avalanche photo-diode detectors were used for the detection of the X-rays originating from the resonance process. The NRIXS detector was placed close to the sample surface in order to detect the characteristic L-fluorescence X-rays emitted by Sn atoms during the process of de-excitation of  $^{119}\text{Sn}$  nuclei to the ground state. The instrumental resolution function was measured simultaneously with the NRIX spectrum by detecting the forward scattered intensity. The measurement time of the NRIXS spectrum was about 1 h. The NRIXS data evaluation and extraction of the VDOS were performed by using the computer program PHOENIX described elsewhere [39]. The thickness of 800 Å of our  $\text{Mg}_2\text{Sn}$  film is sufficiently large, so that the measured VDOS is representative of the bulk material [22–24].

### 5.1. NRIXS results

Figure 8 exhibits the NRIXS spectra (raw data), i.e. the excitation probability *versus* energy transfer  $E$ , of the  $\text{Mg}_2\text{Sn}$  thin film. The spectrum shows the dominant central elastic peak at the nuclear transition energy  $E_0$  (energy transfer  $E=0$  meV) and sidebands at lower and higher energy. X-rays with less energy than  $E_0$  excite the nuclear resonance by net annihilation of phonons (low-energy sideband). The high energy sideband is produced by creation of phonons. The observed asymmetry in the spectrum reflects the “detailed balance” due to the Boltzmann factor [29]. The instrumental resolution function with a FWHM of 0.9 meV is also shown in figure 8. The resolution function is nearly symmetrical and falls off rapidly from the center without having extended wings.

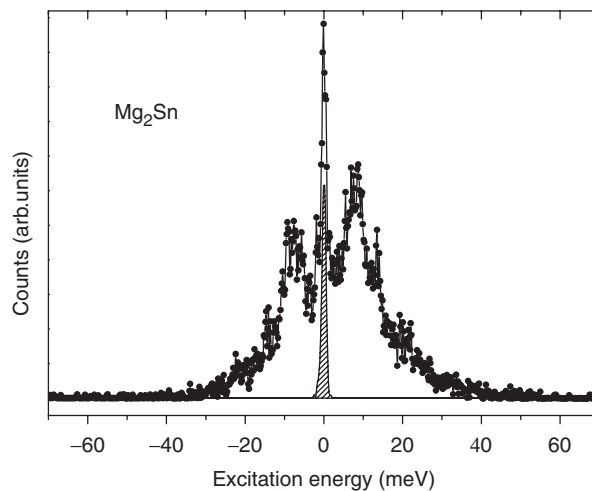


Figure 8.  $^{119}\text{Sn}$  NRIXS spectrum (raw data) of 800 Å thick  $\text{Mg}_2\text{Sn}$  thin film grown at  $T_s = -140^\circ\text{C}$ . The instrumental resolution function is also shown (central peak, shaded curve). The spectrum was taken at  $RT$ .

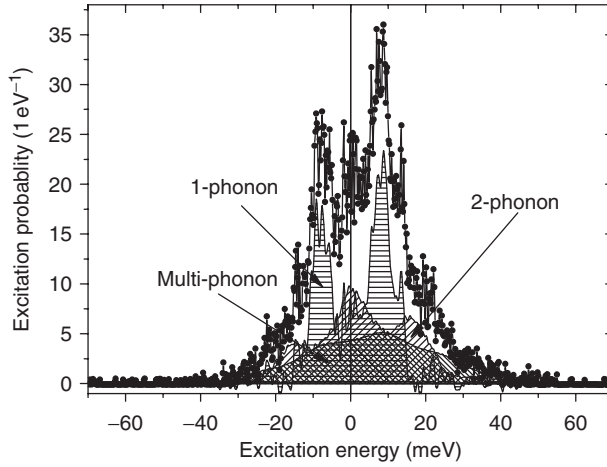


Figure 9. Vibrational excitation probability per unit energy,  $W(E)$ , for the  $\text{Mg}_2\text{Sn}$  thin film at  $RT$ , obtained from the NRIXS spectra of figure 8 after subtraction of the central elastic peak and proper normalization. The contribution of one-phonon, two-phonon and higher-order phonons are also shown.

After subtraction of the central elastic peak from the measured NRIXS spectrum the data were normalized according to the standard procedure [12, 13, 39] yielding the vibrational excitation probability per unit energy,  $W(E)$ , as shown in figure 9. The contribution to  $W(E)$  of inelastic processes in terms of one-phonon, two-phonon and higher-order phonons are also depicted in figure 9. They were obtained according to the procedures described in refs. [12, 13, 39].

By integration of  $W(E)$  over all energies the quantity  $(1-f)$  is obtained in a model independent way, where  $f$  is the Lamb–Mössbauer factor (or  $f$ -factor). The values of the  $f$ -factor of the  $\text{Mg}_2\text{Sn}$  sample at  $RT$ , obtained from the data in figure 9, is given in table 1. In the harmonic approximation the partial VDOS,  $g(E)$ , is proportional to the one-phonon contribution  $S_1(E)$  in  $W(E)$ , and is given by [17, 18]

$$g(E) = \frac{S_1(E)}{E_R} E(1 - e^{E/k_B T}), \quad (1)$$

where  $E_R$  is the recoil energy of the resonating nucleus,  $k_B$  is Boltzmann's constant, and  $E$  is the transferred energy.  $g(E)$  was deduced from the measured distribution  $W(E)$  in figure 9 according to standard procedures [12, 13, 39]. Figure 10(a) exhibits the Sn-projected  $g(E)$  of the  $\text{Mg}_2\text{Sn}$  film.  $g(E)$  is characterized by a dominant peak near 9 meV and a strong peak near 14 meV. Further, a significant peak is observed near 22 meV, which is part of a weaker band extending between about 20 and 28 meV. The features above about 30 meV belong to the noise level. Important thermodynamic quantities can be obtained from the measured  $W(E)$  and  $g(E)$  spectra [17, 39]. Besides the  $f$ -factor we have determined the mean atomic force constant  $V(\vec{s})$  along the beam direction  $\vec{s}$ , the mean kinetic energy per atom  $T(\vec{s})$ , the vibrational specific heat per atom ( $C_v$ ), and the vibrational entropy per atom ( $S_v$ ), all at  $RT$ . These quantities are given in table 1, together with the calculated values of the mean square displacement  $\langle x^2 \rangle$  of the  $^{119}\text{Sn}$  atom, the Debye energy  $E_D$  and the Debye temperature  $\Theta_D$ . The Debye temperature,  $\Theta_D$ , was calculated from

Table 1. Thermodynamic properties of Mg<sub>2</sub>Sn derived from the NRIXS results:  $f$  = f-factor at  $RT$ ,  $f_0$  = f-factor at 0 K (Calc). The mean square displacement  $\langle x^2 \rangle$  (in Å<sup>2</sup>), the Debye energy  $E_D$  (in meV) and the Debye temperature  $\Theta_D$  (in K) were calculated from  $f$  at  $RT$ .  $V(\vec{s})$  = mean atomic force constant (in N m<sup>-1</sup>) at  $RT$ ,  $T(\vec{s})$  = mean kinetic energy (in meV atom<sup>-1</sup>) at  $RT$ ,  $T_0(\vec{s})$  = mean kinetic energy (in meV atom<sup>-1</sup>) at 0 K (Calc),  $C_v$  = vibrational specific heat (in  $k_B$  atom<sup>-1</sup>) at  $RT$ , and  $S_v$  = vibrational entropy (in  $k_B$  atom<sup>-1</sup>) at  $RT$ . The values at  $T=0$  K were calculated from corresponding  $RT$  values according to the Debye model.

$f$	0.20(1)
$f_0$	0.78(2)
$\langle x^2 \rangle$	0.0109(5)
$E_D$	16(1)
$\Theta_D$	182(14)
$V(\vec{s})$	62(53)
$T(\vec{s})$	13.2(7)
$T_0(\vec{s})$	2.9(5)
$C_v$	3.0(1)
$S_v$	5.50(7)

the measured  $RT$  values of the f-factor according to the Debye model with the relation:

$$f = \exp \left[ \frac{-6E_R}{k_B \theta_D} \left( \frac{1}{4} + \left( \frac{T}{\theta_D} \right)^2 \int_0^{\theta_D/T} \frac{x}{e^x - 1} dx \right) \right] \quad (2)$$

where  $E_R = 2.57$  meV is the recoil energy of the <sup>119</sup>Sn nucleus. The f-factor at  $T=0$  K,  $f_0$ , was calculated from the relation  $f_0 = \exp[-3E_R/(2k_B \Theta_D)]$ . The mean kinetic energy at  $T=0$  K,  $T_0(\vec{s}) = M \langle v_0^2(\vec{s}) \rangle / 2 = M \langle v_0^2 \rangle / 6$  (with  $M$  = nuclear mass of <sup>119</sup>Sn) was calculated according to the Debye model using the relation  $\langle v_0^2 \rangle = 9k_B \Theta_D / 8M$  for the mean square velocity of the <sup>119</sup>Sn atom at  $T=0$  K [40].

## 6. Calculated VDOS of Mg<sub>2</sub>Sn

The vibrational dynamics calculations were carried out by using the linear response method [41–43]. In this method the dynamical matrix is obtained from the modification of the electron density via the inverse of the dielectric matrix describing the response of the valence electron density to a periodic lattice perturbation. The dielectric matrix is then calculated from the eigenfunctions and energy levels of the unperturbed system [44]. Phonon dispersions can be determined at any wave vector in the Brillouin zone with the computational effort described by the generalized gradient approximation (GGA). Only linear effects, such as harmonic vibrational excitations, are accessible to this technique. The method has been applied with success to several crystalline alloys related to our present study [45,46].

Phonon dispersion relations (figure 11) along high symmetry directions were calculated for the fcc Mg<sub>2</sub>Sn structures by using the linear response code of plane wave self-consistent field (PWSCF) [47]. The phonon calculations were carried out at the theoretical lattice constant 6.8199 Å. We used ultrasoft pseudopotentials

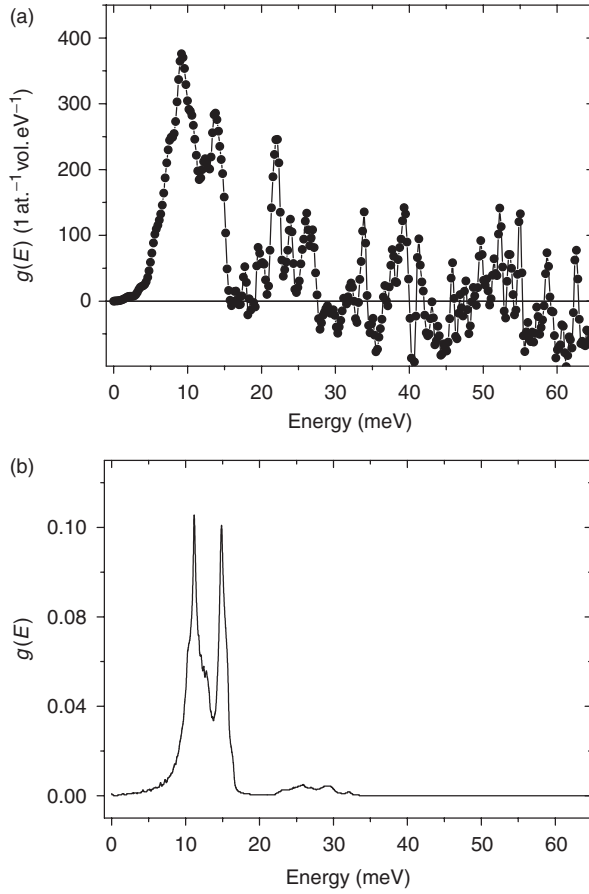


Figure 10. (a) Measured  $^{119}\text{Sn}$ -projected vibrational density of states,  $g(E)$ , at  $RT$  of 800 Å thick  $\text{Mg}_2\text{Sn}$  thin film. Energy resolution  $\Delta E = 0.9$  meV; (b) calculated Sn-projected (partial) vibrational density of states of  $\text{Mg}_2\text{Sn}$ .

introduced by Vanderbilt [48], in a similar way as in ref. [47], with exchange correlation using the Perdew-Wang-91 exchange-correlation functional [49] generated by taking a scalar-relativistic consideration into account. An energy cut-off of 60.0 Ry was used to describe the plane wave basis set, and Fourier components of the charge density with energy up to 600 Ry were taken into account for the calculation of the matrix elements of the system Hamiltonian. The integration over the Brillouin zone (BZ) was performed with  $12 \times 12 \times 12$  k-points generated by the Monkhorst–Pack method with smearing technique suitable for metallic systems. Structural properties and most of the phonon frequencies are well converging by using a first-order smearing parameter  $\sigma = 0.02$  Ry. In order to calculate the force constant matrices and the inverse Fourier transform, we used a set of 8 q-points corresponding to  $4 \times 4 \times 4$  k-points of a (444) uniform grid in the irreducible BZ of the fcc lattice. The total phonon density of states was computed using the tetrahedron method [50], while we used the histogram technique with data smearing to extract the partial phonon density of states.

Our calculated dispersion curves and total VDOS, as shown in figure 11, are very similar to those measured [6] and calculated [6, 9] earlier. Our calculated VDOS

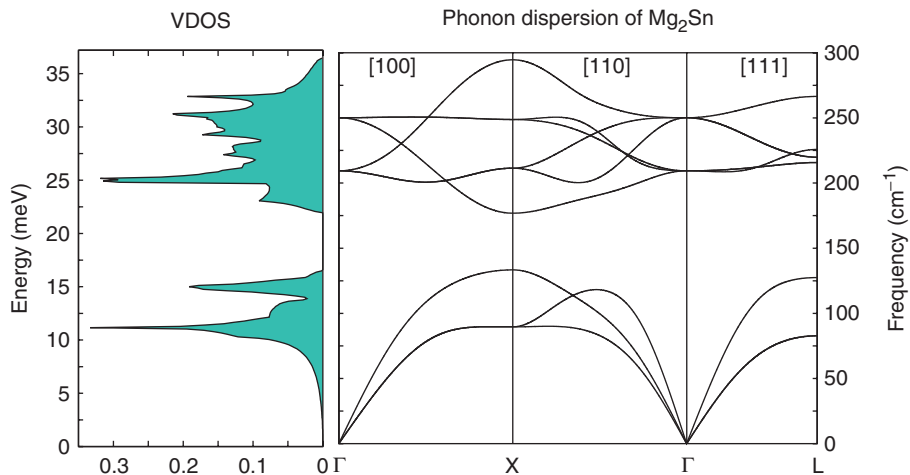


Figure 11. Calculated total vibrational density of states,  $g(E)$ , (left) and phonon dispersion relations (right) for bulk  $\text{Mg}_2\text{Sn}$ .

shows a dominant peak at  $\sim 11$  meV and a strong side peak at  $\sim 15$  meV. A phonon energy gap is observed between  $\sim 17$  and 21 meV. Above the gap, an energy band is found up to  $\sim 35$  meV, including a strong peak at  $\sim 25$  meV.

In figure 10 we compare our experimentally (figure 10a) and our theoretically (figure 10b) obtained Sn-projected VDOS. In the lower energy region the strong two-peak structure in the experimental and theoretical VDOS is very similar. The experimental peak positions at  $\sim 9$  and 14 meV are close to the corresponding theoretical peak positions of  $\sim 11$  and 15 meV. Generally, features in the computed  $g(E)$  are found to be shifted by  $1 \sim 2$  meV towards higher energy as compared with features in the experimental VDOS. This two-peak feature in  $g(E)$  is clearly related to vibrations of the heavier Sn atoms. The experimental Sn-projected VDOS (figure 10a) also reveals the phonon energy gap between  $\sim 15$  and 20 meV, which agrees well with the theoretical gap ( $\sim 17$ –21 meV). For phonon energies above the gap, i.e. in the range  $\sim 22$ –35 meV, the theoretical Sn-projected VDOS (figure 10b) is relatively low. This is in contrast to the experimental  $g(E)$  (figure 10a), where stronger features, in particular a relatively strong peak near 22 meV, is observed in this energy regime. Comparison of the theoretical Sn-projected VDOS (figure 10b) with the computed total VDOS (figure 11) reveals that the phonon band above the gap (energy  $> \sim 22$  meV) originates essentially from vibrations of the lighter Mg atoms. Therefore, it is surprising that a relatively strong band (and even a strong peak near 22 meV) is experimentally found in the Sn-projected VDOS in that energy range. This observation indicates that hybridization of the Sn and Mg vibrational modes occurs in the energy range above the gap, which is more pronounced than predicted by our present theory.

## 7. Summary

A polycrystalline semiconducting  $\text{Mg}_2\text{Sn}$  thin film has been successfully prepared by co-deposition of the elements onto an oxidized Si(100) substrate at  $-140^\circ\text{C}$ .

The semiconducting property of the film was confirmed by electronic transport and infrared-spectroscopical measurements and its electronic band-gap was determined to be  $\sim 0.2$  eV. The  $^{119}\text{Sn}$ -projected (partial) vibrational density of states (VDOS) has been measured by NRIXS of 23.878 keV synchrotron radiation with 0.9 meV energy resolution. The Sn-projected VDOS,  $g(E)$ , and various thermodynamic quantities were deduced from the NRIXS spectra. The theoretically obtained Sn-projected (partial) VDOS is compared with the measured partial VDOS, and reasonable agreement is observed. The VDOS is characterized by a phonon energy-gap ranging from  $\sim 17$ – $21$  meV.

### Acknowledgements

We are grateful to U. von Hörsten (Duisburg) for valuable technical assistance and sample preparation. Work at Duisburg was supported by Deutsche Forschungsgemeinschaft (GRK 277 and SFB 491). Work at Argonne was supported by the US department of energy, Basic Energy Sciences, Office of Science, under Contract No. W-31-109-Eng-38.

### References

- [1] R.F. Blunt, H.P.R. Frederikse and W.R. Hosler, *Phys. Rev.* **100** 663 (1955).
- [2] N. Wakabayashi, A.A.Z. Ahmad, H.R. Shanks, *et al.*, *Phys. Rev. B* **5** 2103 (1972).
- [3] A. Svane and E. Antoncik, *Phys. Rev. B* **35** 4611 (1987).
- [4] K.B. Kaiser and R.J. Kearney, *Phys. Rev.* **162** 716 (1967).
- [5] L.D. Crossman and G.C. Danielson, *Phys. Rev.* **171** 867 (1968).
- [6] R.J. Kearney, T.G. Worlton and R.E. Schmunk, *J. Phys. Chem. Solids* **31** 1085 (1970).
- [7] A. Singh and B. Dayal, *J. Phys. C: Solid St. Phys.* **3** 2037 (1970).
- [8] R.J. Kearney, T.G. Worlton and R.E. Schmunk, *J. Phys. Chem. Solids* **31** 913 (1970).
- [9] L.C. Davis, W.B. Whitten and G.C. Danielson, *J. Phys. Chem. Solids* **28** 439 (1967).
- [10] F.J. Jelinek, W.D. Shickell and B.C. Gerstein, *J. Phys. Chem. Solids* **28** 267 (1967).
- [11] M. Seto, Y. Yoda, S. Kikuta, *et al.*, *Phys. Rev. Lett.* **74** 3828 (1995).
- [12] W. Sturhahn, T.S. Toellner, E.E. Alp, *et al.*, *Phys. Rev. Lett.* **74** 3832 (1995).
- [13] E.E. Alp, W. Sturhahn and T.S. Toellner, *J. Phys.: Condens. Matter* **13** 7645 (2001).
- [14] A.I. Chumakov, R. Ruffer, H. Grünsteudel, *et al.*, *Europhys. Lett.* **30** 427 (1995).
- [15] A.I. Chumakov and W. Sturhahn, *Hyperfine Interact.* **123/124** 781 (1999).
- [16] E.E. Alp, W. Sturhahn and T.S. Toellner, *Hyperfine Interact.* **135** 295 (2001).
- [17] E.E. Alp, W. Sturhahn, T.S. Toellner, *et al.*, *Hyperfine Interact.* **144/145** 3 (2002).
- [18] W. Sturhahn, *J. Phys.: Condens. Matter* **16** S497 (2004).
- [19] W. Sturhahn, R. Röhlberger, E.E. Alp, *et al.*, *J. Magn. Magn. Mater.* **198/199** 590 (1999).
- [20] B. Sahoo, W. Keune, W. Sturhahn, *et al.*, *J. Phys. Chem. Solids* **66** 2263 (2005).
- [21] T. Ruckert, W. Keune, W. Sturhahn, *et al.*, *Hyperfine Interact.* **126** 363 (2000).
- [22] W. Keune and W. Sturhahn, *Hyperfine Interact.* **123/124** 847 (1999).
- [23] T. Ruckert, W. Keune, B. Sahoo, *et al.*, *Hyperfine Interact.* **144/145** 65 (2002).
- [24] W. Keune, T. Ruckert, B. Sahoo, *et al.*, *J. Phys.: Condens. Matter* **16** S379 (2004).
- [25] B. Roldan Cuenya, W. Keune, W. Sturhahn, *et al.*, *Phys. Rev. B* **64** 235321 (2001).
- [26] T. Ruckert, W. Keune, W. Sturhahn, *et al.*, *J. Magn. Magn. Mater.* **240** 562 (2002).
- [27] J.A. Gomez, D. Guenzburger, D.E. Ellis, *et al.*, *Phys. Rev. B* **67** 115340 (2003).
- [28] M. Walterfang, W. Keune, E. Schuster, *et al.*, *Phys. Rev. B* **71** 035309 (2005).
- [29] W. Sturhahn and V.G. Kohn, *Hyperfine Interact.* **123/124** 367 (1999).
- [30] R.A. Brand, *Nucl. Instrum. Methods B* **28** 398 (1987).
- [31] J.G. Stevens, *Hyperfine Interact.* **13** 221 (1983).

- [32] J.G. Stevens and V.E. Stevens (Editors), *Mössbauer Effect Data Index Covering the 1974 Literature*, (IFI/Plenum, New York, Washington, London, 1975), p. 152.
- [33] R. Tilley, *Understanding Solids: The Science of Materials*, John Wiley & sons Ltd, England, (2004).
- [34] H.P.R. Frederikse, W.R. Hosler and D.E. Roberts, *Phys. Rev.* **103** 67 (1956).
- [35] L.J. van der Pauw, *Philips Tech. Rev.* **20** 220 (1958/59).
- [36] J. Umeda, *J. Phys. Soc. Japan* **19** 2052 (1964).
- [37] B.D. Lichter, *J. Electrochem. Soc.* **109** 819 (1962).
- [38] H.G. Lipson and A. Kahan, *Phys. Rev.* **133** A800 (1964).
- [39] W. Sturhahn, *Hyperfine Interact.* **125** 149 (2000).
- [40] G.K. Shenoy, F.E. Wagner and G.M. Kalvius, in: *Mössbauer Isomer Shifts*, edited by G.K. Shenoy and F.E. Wagner (North Holland, Amsterdam, Newyork, 1978), p. 49.
- [41] P. Giannozzi, S. de Gironcoli, P. Pavone, *et al.*, *Phys. Rev. B* **43** 7231 (1991).
- [42] S. Yu. Savrasov, *Phys. Rev. Lett.* **69** 2819 (1992)
- [43] S. Baroni, S. de Gironcoli and A.D. Corso, *Rev. Mod. Phys.* **73** 515 (2001)
- [44] R. Resta, *Rev. Mod. Phys.* **66** 899 (1994)
- [45] A.D. Corso and S. de Gironcoli, *Phys. Rev. B* **62** 273 (2000).
- [46] C. Bungaro, K.M. Rabe and A.D. Corso, *Phys. Rev. B* **68** 132402 (2003).
- [47] S. Baroni, S. de Gironcoli, A.D. Corso, *et al.*, <http://www.pwscf.org>.
- [48] D. Vanderbilt, *Phys. Rev. B* **41** 7892 (1990).
- [49] J.P. Perdew and Y. Wang, *Phys. Rev. B* **45** 13244 (1992).
- [50] G. Lehmann and M. Taut, *Phys. Stat. Sol. B.* **54**(2) 469 (1972).